Atmospheric Precipitable Water and its Correlation with Clear Sky Infrared Temperature Observations

Vicki Kelsey[1], Sarah Riley [2], and Kenneth Minschwaner [2]

[1]Langmuir Laboratory for Atmospheric Research, New Mexico Institute of Mining and Technology, Socorro, NM 87801 USA
Now at the Atmospheric and Environmental Sciences Program, South Dakota School of Mines and Technology, Rapid City, SD 57701 USA
[2]Department of Physics, New Mexico Institute of Mining and Technology, Socorro, NM 87801 USA

Correspondence: Vicki Kelsey (vicki.kelsey@mines.sdsmt.edu)

Abstract. Total precipitable water (TPW) in the atmosphere is the vertically integrated amount of atmospheric water in all of its phases. TPW is a valuable predictor for weather forecasting, and it is routinely measured using radiosondes, ground-based global positioning systems (GPS), sun photometers, or microwave radiometers. The use of these sophisticated instruments limits the number of TPW measurement sites, which affects the accuracy of forecast models in regards to storm formation,

5 strength, and the potential for precipitation. We have analyzed this relationship for the much drier climate zone found in the Desert Southwest, specifically over Socorro, New Mexico (34°N, 107°W). Daily measurements of the ground and zenith sky temperatures have been made at Socorro for two complete annual cycles using infrared thermal sensors. Radiosonde TPW measurements from National Weather Service stations located in nearby Albuquerque, and Santa Theresa, New Mexico, are input into our dataset and analysed via a newly developed computational tool. Our results show that an exponential relationship between TPW and zenith sky temperature also holds for the Desert Southwest, but with parameters that are different than

10 those obtained for the Gulf Coast. Model simulations can accurately reproduce the observed relationship between TPW and temperature, and the results suggest that half of the signal in temperature is directly related to direct changes in opacity due to changes in TPW, while the other half is due to changes in air temperature that usually accompany changes in TPW.

1 Introduction

15 The amount of water in the atmosphere is an important factor that can, along with other factors, determine the amount of rainfall and influence the dynamical evolution of convective storms.. When the vertically integrated amount of water (Total Precipitable Water, or TPW) is more than twice the climatological amount, heavy precipitation can occur (Wang et al., 2017), which may lead to soil erosion and flooding. Weather forecasting is dependent upon having accurate TPW data with sufficient temporal/spatial coverage over the forecasting area (Yang and Smith, 2018; Marcus et al., 2007). Although TPW can

20 be obtained from infrared measurements on satellite platforms such as GOES-R (Schmit et al., 2018, 2017), potentially large observation angles can result in degraded spatial resolution, and may not provide adequate information for numerical weather prediction models to take into account local variations in TPW. Building upon a method using low-cost materials to determine TPW based on infrared temperature measurements of the zenith sky (Mims et al., 2011), we examined whether similar tech-

niques could also be applied for higher elevation, arid and semiarid regions. A better understanding of this methodology may
25   also demonstrate the feasibility of a citizen observer network, which could supply temperature data that would help monitor
the TPW variations across different locations in a region. Increasing the availability of TPW data will ensure more accurate
forecasts; especially in higher elevation arid climate zones where there are large distances between existing TPW measurement
sites (Maussion et al., 2014; Chen et al., 2018; Zhao et al., 2019).

TPW strongly influences atmospheric dynamics. This is most evident in the fact that when large amounts of TPW are ob-
30   served, there is a greater probability for uplifting convection and cloud formation (Raj et al., 2004). This leads to applications
in numerical weather prediction (Wang et al., 2007), as well as climate change modeling and analysis (Gradinarsky et al.,
2002). Higher amounts of TPW tend to be located near the equator and especially near Intertropical Convergence Zones, with
a general decrease in TPW from low to high latitudes (Raj et al., 2004).

In this paper we use the standard definition of TPW (Salby, 1996), which is determined by the integrated amount of water
35   that is contained in a vertical column of air extending from the Earth's surface to the top of the atmosphere, typically expressed
as the height of the liquid water equivalent. Under clear skies that are the main focus of our work, all of this water is in vapor
form and the expression becomes

$$\text{TPW} = \frac{1}{\rho g} \int_0^{p_o} \mu(p) dp, \tag{1}$$

where ρ is the mass density of liquid water, g is the acceleration of gravity, $\mu(p)$ is the mass mixing ratio of water vapor, and
40   the integral is over pressure p from zero to some surface pressure p_o.

Typically, the water vapor mass density decreases quasi-exponentially with increasing altitude (decreasing pressure), such
that the majority of the total column is near the surface. Previous studies have determined that 40% to 60% of the contribution
to sea-level TPW occurs in the pressure layer between 1000 hPa and 850 hPa, with roughly 90% lying between the surface
and 500 hPa (Ross and Elliott, 1996; Wang et al., 2007; Raj et al., 2004). Here we will emphasize the importance of surface
45   elevation on TPW due to the high desert elevation of the Socorro measurement site. As most previous studies have focused on
lower surface elevations and tropical environments, there remains a need to easily determine the TPW in high elevation arid
climate zones for improved forecasting and trend monitoring.

1.1   Current methods of measuring TPW

There currently exist several methods for directly and indirectly measuring the total impact of water vapor in the atmosphere.
50   The more traditional methods of measuring this impact include: Radiosondes, ground-based Global Position System signal
delay analysis, Solar Photometry, and Microwave Radiometry. Though each method has proven successful, the radiosonde
remains the most widely used method to obtain atmospheric data. Some of the limitations of using Radiosondes to study the
atmosphere include the cost of balloons and sensors, availability of personnel and launch sites, and the frequency of launches.

Global Positioning Systems utilize a signal that passes through the atmosphere from a satellite to a ground-based receiver,
55   which measures the delay as a result of the amount of water vapor along the atmospheric path between the receiver and the

satellite (Means and Cayan, 2013). This signal delay can be used to estimate TPW assuming spatial homogeneity in conversion to a vertical column of air. Measurement sites are primarily located near major airports, and therefore do not supply rural TPW measurements.

Solar photometric methods apply a Langley extrapolation of multi-channel radiometric data in order to quantify TPW. Sun photometers utilize both the 940 nm and 1020 nm near-infrared bands to determine TPW (Raj et al., 2004). Relative to radiosonde data, this collection technique records TPW data with a precision of about 10%. (Thome et al., 1992; Thomason, 1985).

Microwave Radiometers use Gigahertz frequencies to measure the incident microwave energy in the atmosphere, wherein the 23.8 GHz frequency is three times more sensitive to the concentration of atmospheric water vapor relative to the 31.4 GHz frequency (Liljegren, 1994). This two-channel approach enables a comprehensive profile of tropospheric water vapor and liquid water (Hogg et al., 1983). Limitations to using microwave radiometers to measure TPW include interference noise.

Our research builds on from principles developed in previous work that suggested the use of low-cost thermal sensors for monitoring TPW, as quantified by an exponential relationship between TPW and zenith sky temperatures over the Gulf Coast of Texas (Mims et al., 2011). For the remainder of the paper, we will discuss the observational methods including sensors and derivation of TPW from radiosondes (Sect. 2), results and analysis (Sect. 3), and interpretation using model simulations (Sect. 4). Conclusions are presented in Sect. 5.

2 Observational methods

We utilize infrared thermometry to measure the zenith sky (vertically upward at zenith angle of zero) temperature with a temporal resolution of approximately one day over Socorro, New Mexico (34N, 107W, 1.42 km surface elevation)(Kelsey and Riley, 2021). Three different handheld thermal sensors were used in this study: TE 1610[1], FLIR i3, and AMES.

2.1 Sensors

The TE 1610 sensor has a temperature measurement range of -20°C through 537°C. Attempts to determine the infrared wavelength band that this sensor operates in were inconclusive due to the lack of clear sky data available. The error for temperature readings, as determined by the manufacturer, is ±2.5°C.

The FLIR i3 sensor has the capacity to measure temperatures ranging from -20°C to 250°C (however, in our observations this sensor has produced temperature readings down to -40°C). The manufacturer defines the accuracy of these measurements as ±2°C and defines the spectral sensitivity to be between 7.5 and 13 μm (FLIR Systems Inc., 2012). Compared to the 4.8° conical field of view associated with the TE 1610 and AMES thermometers, the FLIR i3 has a 12.5°×12.5° rectangular field of view.

Finally, the AMES thermometer can measure temperatures from -50°C to 550°C. The manufacturer error associated with

---

[1]As a result of the lack of viable data from the TE 1610 (2 measurements out of 539 days), we have removed this sensor from further analysis and comparison.

this instrument differs between two temperature ranges. The first is between -50°C and 0°C, with an error of ±3.9°C (Harbor Freight Tools, 2017). The second range is 0.5°C and 550°C, the error for this range is ±2.2°C (Harbor Freight Tools, 2017). In our measurements we have found few instances where the temperature reading is below the -50°C threshold. There is not a defined spectral range provided by the manufacturer for this sensor. However, we inferred that the spectral sensitivity of the sensor lies within the range 7μm - 10μm by comparing to radiative model calculations as further discussed in Sect. 4. We employed two sensors of this type: AMES 1, which was used starting on 22 January 2019, and AMES 2 which was put into service on 14 May 2019.

2.2 Measurement procedure

As discussed previously, the zenith sky temperature measurements are taken once a day, typically near 1700-1800 UTC or 2300-2400 UTC to avoid having the sun within the field of view of the sensors. Sky temperature is measured at the zenith to facilitate the measurement of the vertical column air temperatures. This ensures the shortest optical path is used for infrared water vapor measurements (Smith and Toumi, 2008). A series of measurements were taken to investigate the impact of manual observations having small offsets from true zenith, where readings were taken at varying angles up to 30° off of zenith over a week-long period. It was determined that with proper technique one can manually get within 5° of true zenith, which introduces less than 1°C variation in clear sky temperature measurements. We also measure the immediate ground temperature as a check on instrument calibration and drift.

The presence of clouds, smoke, dust, or aerosol within the sensor field of view can have an impact on observed sky temperatures. Clouds, in particular, are capable of affecting the observations by providing an effective emission source at temperatures near cloud base. We screen and exclude any observations contaminated by clouds. Figure 1 shows the breakdown of sky conditions and sensor readings for the entire data record. We find that cloud screening results in the loss of data for about 25% of daily readings. Additionally, there are occasions when a given sensor will not produce a reading (NaN) when the sky temperature falls below the calibrated range for that sensor. This occurs mostly under clear skies, and it varies from 2% of the measurements for AMES 2 to 50% for FLIR i3 (Fig. 1). The larger fraction of NaN days for the FLIR i3 instrument is likely due to a warmer low-temperature cutoff (-40°C for FLIR i3 versus -50°C for AMES), and a different spectral sensitivity that is closer to the transparent atmospheric window between 8 and 12 μm wavelength. We have not made any measurements in the presence of noticeable smoke or dust. Surface solar radiation measurements at Socorro have shown that aerosol optical depths are typically very low, varying between 0.03 and 0.10 with maximum values during summer (Minschwaner et al., 2002). Variations in aerosol are not considered here, but they will contribute a small additional source of variability in sky temperature readings.

2.3 Infrared opacity and instrument comparison

As discussed above, the spectral sensitivity curves for each of our thermal sensors are not precisely known, but they are all assumed to have passbands that fall within relatively transparent atmospheric windows at wavelengths between ∼7 to ∼12 μm, corresponding roughly to the mid-IR spectral range. The downward mid-IR radiance observed at ground level with clear skies
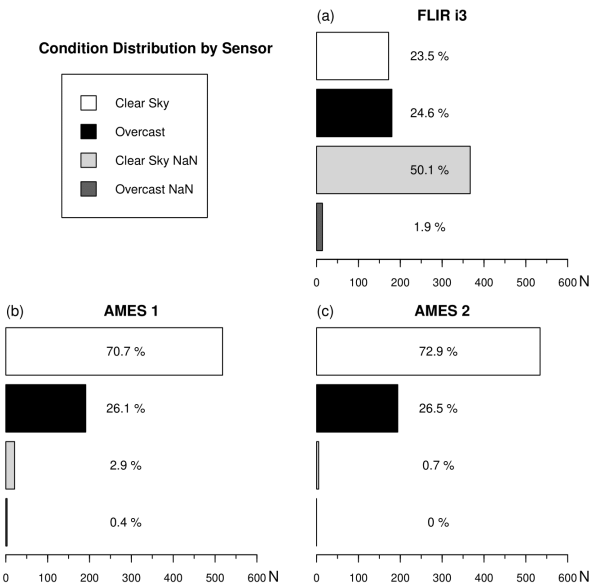
Figure 1. Fractional distribution of measurement conditions for each sensor, with FLIR i3 (a), AMES 1 (b), and AMES 2 (c). White bars indicate the fraction of measurements obtained under clear sky conditions, black bars are the fraction of measurements made in the presence of clouds, light gray bars represent the fraction of measurements falling outside of the sensor's range under clear skies (NaN readings), and dark gray bars are cases of NaN with cloudy skies.

is primarily dependent on the vertical distribution of atmospheric temperature, and on the vertical distributions of greenhouse
120   gases with mid-IR absorption signatures (e.g. Thomas et al. (1999)). The most important infrared-active gases at these wave-
lengths are ozone, with a vibrational band at 9.6 μm, and water vapor, with a weak continuum between the 6.3 μm vibrational
band and the far-IR rotational lines of H_2O (Stephens, 1994). Although the 9.6 μm ozone feature is significant for transmission
through the entire atmosphere, most of the ozone is located in the stratosphere and ozone generally has a negligible impact
on mid-IR transmission for path lengths within the lowest few kilometers of the surface, except perhaps under highly polluted
125   conditions. On the other hand, even though the H_2O continuum absorption is considered weak (only 10%-20% absorption
through the entire atmosphere), the radiative effects can be significant for path lengths near the surface. The magnitude of this
so-called e-type absorption varies as the square of the absorber amount (e.g. Burroughs (1979)). Furthermore, the scale height
for the vertical distribution of water vapor ($\sim$3 km) is much smaller than for the background atmosphere, so that most of the
water vapor continuum effects are felt within the lowest few kilometers of the surface.
130   Figure2 shows instrument comparisons for clear sky temperatures and for ground temperatures, where the AMES 1 instru-
ment is used as a standard due to its longevity and stability during the course of observations. We find that the AMES 1 and
AMES 2 instruments agree to within $\pm$ 2°C for both ground and sky temperatures, with no clear bias or offset. The FLIR
i3 and AMES 1 instruments are also in good agreement for ground temperature, but they show a considerable difference in
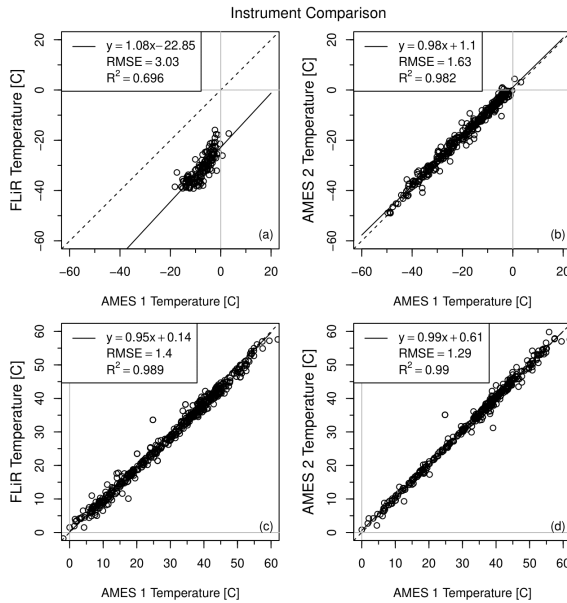
Figure 2. (a,c) Comparison of temperatures between the FLIR i3 and the AMES 1 sensors for the clear zenith sky (a), and the ground (c). A 1:1 line is indicated as a dashed black line with the linear least-squares fit represented as a solid black line. (b,d) Same as left column but for the AMES 2 and AMES 1 sensors.

sky temperature. The FLIR i3 sensor consistently obtains readings that are $\sim 20^{\circ}$C cooler than AMES 1 temperatures, and the

135 difference grows larger with decreasing temperature. We believe that these differences are largely due to the difference in spectral passbands between the FLIR i3 and AMES sensors, with the FLIR i3 passband lying closer to the 8-12 μm atmospheric window, where water vapor opacity is a minimum and the effective emission occurs at higher altitudes and cooler temperatures, as shown in Appendix A. For these reasons and because of the differences in low-temperature cutoffs between the FLIR i3 compared with the other two sensors, the FLIR dataset is not included in our analysis.

140 **2.4 TPW determination**

There are no routine precipitable water measurements at Socorro, thus we must utilize balloon soundings from the National Weather Service (NWS) monitoring stations in both Albuquerque (ABQ) and Santa Teresa (EPZ) in order to estimate TPW at Socorro. The ABQ NWS station is located approximately 110 km to the north of Socorro, while EPZ is located about 240 km to the south. Soundings from each station are initiated at 0000 and 1200 UTC, which approximately brackets the $\sim$1800 UTC

145 Socorro temperature measurements; therefore, we average the 0000 and 1200 UTC soundings from each station to obtain daily means. There is generally a good correspondence between ABQ and EPZ daily-mean TPW (ΔTPW/TPW < 20%), consistent with previous studies that show spatial scales for TPW variations on the order of hundreds of kilometers (Randel et al., 1996). However, larger differences between the two stations can be observed during periods when sharp gradients in humidity exist

over central/southern New Mexico. In all of the analysis that follows, we use an unweighted mean of ABQ and EPZ TPW to
150   estimate TPW over Socorro. Sensitivity tests using weighted means (to account for differences in distance to each station), or
using results from the closest station alone (ABQ) do not improve the goodness of fit between observed sky temperature and
TPW. Nevertheless, it should noted that this spatial/temporal averaging will introduce an additional source of uncertainty and
scatter to the TPW dataset derived for Socorro.

3   Results and analysis

155   ### 3.1   Time series

A time series of two years of daily clear sky temperature and precipitable water is shown in Fig. 3. Both quantities show large
seasonal cycles with maximum temperatures and TPW during the late summer and early fall (July-September). The seasonal
amplitude in TPW is very large, with values averaging 5 mm during December-February and peaking at 25-30 mm in August.
This pattern is consistent with the timing of the North American Monsoon in New Mexico. The corresponding zenith sky
160   temperatures range from -40°C in winter to -10°C in late summer. The day-to-day variability is on the order of 2-5 mm for
TPW and roughly 2-5°C for temperature. Note the difference in TPW between Spring-Summer 2019 and Spring-Summer
2020, which provides some measure of the interannual variability. A detailed analysis of seasonal and interannual variability
is beyond the scope of this paper; however, Appendix A presents evidence indicating that some of these differences are related
to large scale changes in relative humidity.

165   ### 3.2   Analytical techniques

For the purpose of this experiment we developed a computational utility to analyze and visualize the collected data. Some of
the visualizations used in the model include temperature and TPW measurements (as a function of time), direct sky temperature
and TPW comparisons, and sensor performance comparisons. The tool implements common numerical methods to study the
exponential relationship between the collected zenith sky temperature and TPW with ease (Riley and Kelsey, 2021). In the
170   development of this computational model, we applied two common numerical methods: linearization of an exponential and
least-square linear regression (LSLR).

We begin the process of analyzing the collected data by purging data that is not viable; this includes out-of-range temperature
readings in addition to incomplete precipitable water measurements. Sensor malfunctions on radiosondes contribute to the
missing precipitable water measurements. Since the FLIR i3 may not produce reliable measurements below its temperature
175   threshold, we have assigned these temperature measurements as not-a-number, and thus are not processed in the final analysis.
As part of this procedure, 4 additional days were not included in the final analysis because the results from these days exceeded
a 3σ limit of deviation from the rest of the entire dataset.

After the data has been pre-processed, the relationship between the zenith sky temperature and precipitable water is passed
through a least-squares linear regression algorithm in $(T_b,\log(TPW))$, resulting in the solid black exponential curve in Fig. 4.
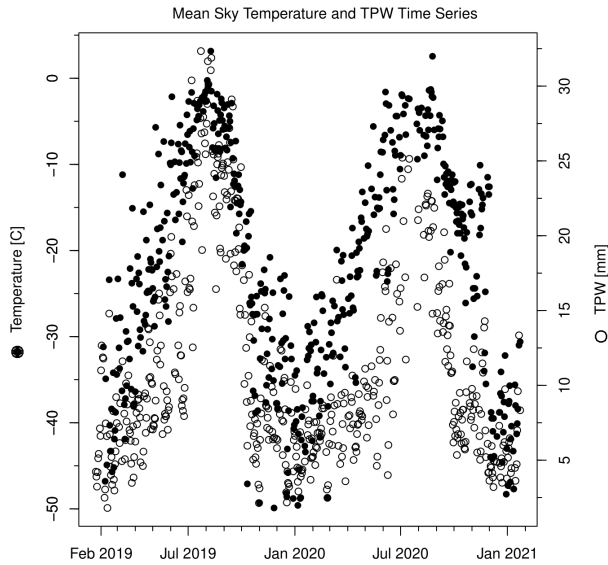
Figure 3. Time series composite of sky temperature (black) and precipitable water (white) over the period from January 2019 through January 2021.

180 The exponential parameters for the best-fit function, physically defined as

$$\text{TPW} = Ae^{BT_b} , \tag{2}$$

as noted in Fig. 4, are $A = 20.86$ mm and $B = 0.036°\text{C}^{-1}$. The confidence interval, denoted as a dashed line, represents the variance of the parameters associated with the best-fit. The prediction interval, denoted as the shaded region, represents specific probability of future data points.

185 The goodness of fit in Fig. 4 confirms that a quasi-exponential relationship between the two variables provides a valid description of these observations. The coefficient of determination (R^2) associated with this relationship is 0.661. Thus, based on the scheme defined by Schober et al. (2018), the correlation described by the model is considered to be strong. The scatter shown in Fig. 4 is dominated by the errors in TPW introduced by spatial/temporal averaging of radiosonde sounding from ABQ and EPZ, with additional contributions from the precision (2-4°C) in the zenith sky temperature measurements and 190 from variations in other atmospheric properties such as aerosol optical depth (estimated at ∼5% in radiance, or about 2°C in brightness temperature).

3.3 Error analysis

The primary sources of error that could have impacted our results include the errors of the sensors, both the thermometers and the radiosondes. As we have discussed in Sect. 2, we have stated that the error for the temperature range that closely resembles
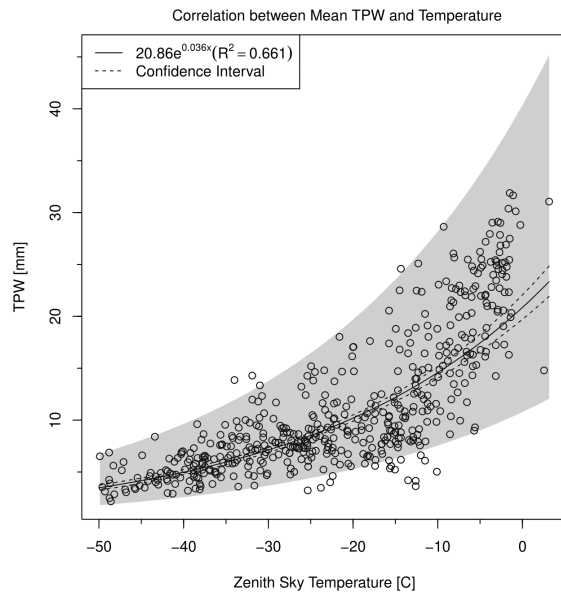
Figure 4. Analytical results of relationship between total precipitable water and zenith clear-sky temperature. Individual days are plotted with white circles. The solid black curve indicates a best-fit exponential relationship; this includes the 95% prediction interval of the data (shaded region) and the 95% confidence interval of the best fit (black dashed curves).

the clear sky is $\pm2°C$ and $\pm3.9°C$ for FLIR i3 and AMES respectively.

The residual standard deviation produced by the LSLR was calculated to be 0.335. We can make note that the data fits within roughly one factor of the standard deviation in Fig. 5.

4 Interpretation and comparison to model simulations

In this section, we interpret the observed relationship between TPW and zenith sky temperature using radiative transfer calculations with the MODTRAN6 (MODerate resolution atmospheric TRANsmission 6) model (Berk et al., 2014). This framework inputs vertical profiles of temperature, density, and radiatively active trace gases, and computes atmospheric spectral transmittances and radiances over a wide spectral range from the ultraviolet through far infrared wavelengths. Here, we focus on vertical path lengths through a midlatitude summer atmosphere (Anderson, 1986), with a surface located at 1.42 km altitude, in order to simulate the zenith sky radiances at Socorro. In the base simulation, TPW = 11.4 mm and the temperature distribution is unchanged from the midlatitude summer case. Other model runs include changes to the TPW by uniformly scaling the water vapor vertical profile by factors of 0.5 and 2 while keeping temperature fixed, and by uniform temperature changes of -5 K and +5 K while keeping TPW fixed.

Figure 6 shows downward spectral radiances computed within a wavelength range between 7 and 10 μm. This range is
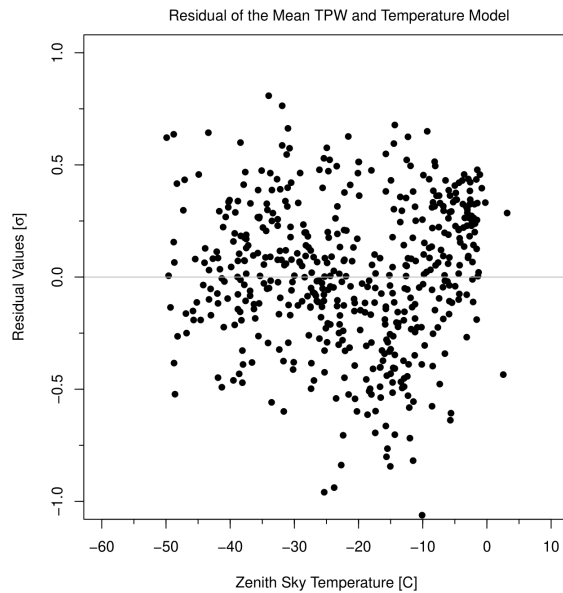
Figure 5. The relationship between the observed sky temperature and the residual values from the regression analysis shown in Fig. 4. The residual values are calculated from the difference between the observed and fitted values of the dependent variable, in this case TPW (Taylor, 1997).

taken for the sake of illustration because, as noted previously, the spectral passband of the AMES thermal sensor is expected

210   to approximately correspond to this region. The radiances shown in Fig. 6 can be used to separately quantify the impact of changes in temperature or water vapor on downward radiances. We find that changes in TPW have the largest relative impact on spectral radiances at 10 μm as compared to 7 μm, due largely to saturation effects closer to the edge of the strong H_2O 6.7 μm band absorption. Changes in temperature, however, have a more uniform spectral effect.

For each case, we integrated the spectral radiances from 7 to 10 μm and determined the equivalent brightness tempera-

215   ture across this spectral range. The equivalent brightness temperature was found by integrating the Planck function over the same spectral range, and solving for the blackbody temperature that provided the same integrated value as the MODTRAN6 downward radiances. The equivalent brightness temperature is intended to simulate our thermal sensor's zenith sky temperature reading, and as indicated in Fig. 6, we do find a relationship between TPW and equivalent brightness temperature that is somewhat consistent with the observations shown in Fig. 4. Higher TPW amount leads to higher effective temperatures,

220   which can be interpreted as a simple lowering in altitude of the effective emission level due to increasing opacity from water vapor, and lower altitudes generally correspond to higher temperatures. For atmospheric temperature, we find an expected increase/decrease in equivalent brightness temperature when atmospheric temperatures are respectively increased/decreased.

We developed a simple linearized model to further interpret our observations using the MODTRAN6 calculations above. If the equivalent brightness temperature, T_b, is assumed to be a function primarily of TPW and atmospheric temperature, T_{air},

225 then

$$\frac{dT_b}{d(\text{TPW})} = \frac{\partial T_b}{\partial(\text{TPW})} + \frac{\partial T_b}{\partial T_{\text{air}}} \cdot \frac{\partial T_{\text{air}}}{\partial(\text{TPW})} \ . \tag{3}$$

The observed relationship between T_b and TPW is clearly nonlinear, but for small changes about some basic state ($T_b \simeq -20°\text{C}$ and TPW $\simeq 11$ mm) we assume that the observations can be represented by the left-hand side of Eq. (3) and that the slope is approximately constant with a magnitude of about $1.9°\text{C mm}^{-1}$ (Fig. 4). The MODTRAN6 simulations can be used to

230 estimate the partial derivative terms, so that the first term on the right-hand side of Eq. (3) has a magnitude of $1.04°\text{C mm}^{-1}$ based on Fig. 6. This is the direct effect of changes in TPW on equivalent brightness temperature, and the results can be shown to capture some, but not all, of the variations in the observed relationship. The second term on the right side of Eq. (3) accounts for changes in T_b that may arise from any coupling between T_b and TPW due to changes in atmospheric temperature, and it is composed of two factors. The first factor is 0.87 based on the MODTRAN6 calculations (Fig. 6). The second factor may

235 be estimated by assuming that the atmosphere maintains a state of constant relative humidity, so that the water vapor partial pressure at all levels (and hence TPW) is set by the Clausius–Clapeyron relation,

$$\frac{de_s}{dT_{\text{air}}} = \frac{L_v}{R_v T_{\text{air}}^2} \ , \tag{4}$$

where e_s is the saturation vapor pressure, L_v is the latent heat of vaporization, and R_v is the specific gas constant for water vapor. If relative humidity is held fixed, then it can be shown that

240 $$\frac{\partial(\text{TPW})}{\partial T_{\text{air}}} = \frac{L_v}{R_v T_{\text{air}}^2} \cdot \text{TPW} \ . \tag{5}$$

Evaluating this equation for $T_{\text{air}} = 273$ K and TPW=11.4 mm, we find the second factor on the far right side of Eq. (3) to be $1.21°\text{C mm}^{-1}$, hence the entire second term has a magnitude of $1.05°\text{C mm}^{-1}$. We conclude that the magnitudes of the two terms on the right side of Eq. (3) are nearly identical at about $1°\text{C mm}^{-1}$, implying an overall slope on the order of $2°\text{C mm}^{-1}$, which is in close agreement with the observed slope of $1.9°\text{C mm}^{-1}$. A comparison of the model results to the

245 observations is shown in Fig. 7. Despite the use of a simple linearized model to describe a clearly nonlinear relationship seen in the observations, we find a good level of agreement that confirms our hypothesis for the two primary influences on the relationship between TPW and zenith sky temperature.

In order to test the robustness of assumptions implicit in Eq. (5). we investigated the relationship between TPW and air temperatures near 3 km altitude using the Albuquerque sounding data spanning over one year. There was a considerable degree

250 of scatter but TPW and air temperature were found to be well correlated, and a linear fit to the data (not shown) produced a slope consistent with the value estimated using Eq. (5). Figure 7 also includes the temperature-TPW relationship fit to observations by Mims et al. (2011), which employs an exponential form somewhat similar to ours. While the overall patterns are similar and consistent with the model, there are differences between the two fits that are most likely due to different sensitivities between the sensors used, and to differences between climate regimes (e.g., mean relative humidities for our location are much lower

255 than for the Mims et al. (2011) study).
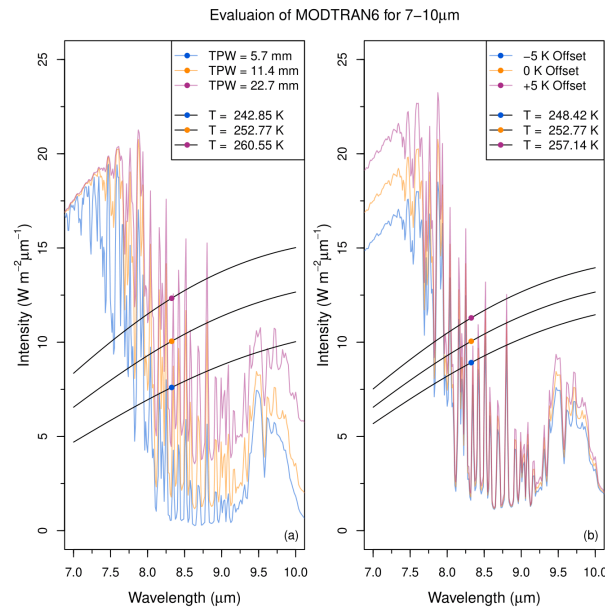
Figure 6. (Left) Downward radiances at the surface, located 1.42 km above sea level, computed using MODTRAN6 with a midlatitude summer model atmosphere. Water vapor was uniformly scaled to produce a TPW of 5.7 mm (blue), 11.4 mm (orange), and 22.7 mm (purple), with all other model parameters held constant. Also plotted are blackbody curves for three different temperatures (black), with each curve having the same integrated radiance as the corresponding MODTRAN6 radiance (T_b=260.55 K, 252.77 K, and 242.85 K for TPW=22.7 mm, 11.4 mm, and 5.7 mm, respectively). (Right) Same as Left but for uniform changes in atmospheric temperature of ± 5 K with water vapor held constant at TPW=11.4 mm. Equivalent blackbody temperatures are T_b=257.14 K, 252.77 K, and 248.42 K for the case of ΔT_b=+5 K, 0 K, and -5 K, respectively.

5 Conclusion and future directions

Our results demonstrate the feasibility of using low-cost (under $50 USD) sensors to measure TPW in less than five minutes using simple measurement protocols, confirming the findings by Mims et al. (2011), but our work extends the previous analysis by observing at colder zenith sky temperatures (down to -40°C) and correspondingly lower TPW (down to ∼3 mm).

260 Our measurements also show that the exact T_b - TPW relationship will be a function of instrument spectral sensitivity and local conditions such as surface elevation and mean relative humidity. In addition, we developed a simple model that uses MODTRAN6 radiative transfer calculations to quantify how T_b can be influenced by changes in TPW and in mean-column air temperature. The model analysis indicates that the observed relationship between zenith sky temperature and TPW can be explained primarily by two dominant influences. First, an increase in TPW leads to increasing atmospheric opacity and a lower

265 altitude for the effective emission height as viewed from the surface. Under typical conditions a lower height corresponds to a higher temperature. Second, an increase in TPW is typically correlated with higher air temperatures; although relative humidity is not perfectly constant, the climatology is such that positive relationships between temperature and humidity are generally
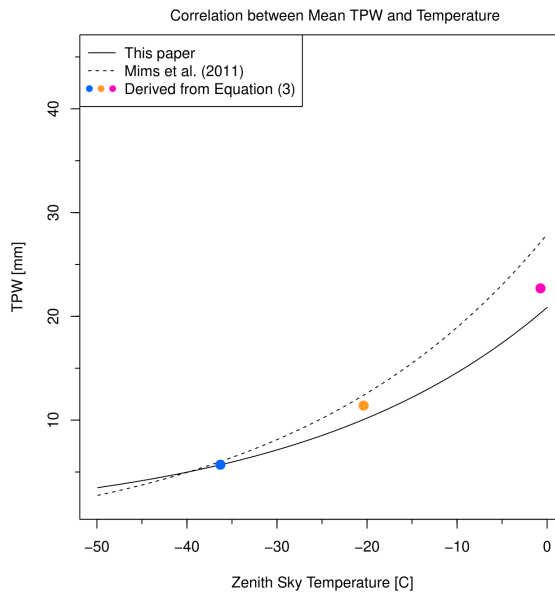
Figure 7. Zenith sky temperature versus TPW for the best fit to measurements from this study (solid curve), best fit from Mims et al. (2011) using the expression $30.55e^{0.035x} - 2.63$ (dashed curve). Results from MODTRAN6 radiance calculations for average 7-10 μm effective brightness temperature (blue, orange, and purple solid circles) are plotted for comparison. The model results include the combined effects of changes in TPW and air temperature on the effective brightness temperature, as expressed by Eq. (3).

observed. Higher air temperatures, in turn, increase the observed zenith sky temperature due to greater emission rates governed by the Planck function, as seen in the MODTRAN6 simulations. The model results show that surface elevation and climato-

270 logical relative humidity are two of the most important local factors in shaping the exact form of the T_b - TPW relationship.

Since TPW can typically be measured to within $\pm20\%$ using this approach with a single-design sensor, it shows promise for applications involving a dense network of TPW observations, and it may be a good candidate for broader observations employing the "citizen science" methodology. Coordinated observations within the Global Learning and Observations to Benefit the Environment (GLOBE) Program has been proven to be successful for a wide variety of geophysical phenomena (e.g., Robles

275 et al. (2020)). The question of whether or not sensors of the same model and manufacturer are similar enough to be used in an observing network is an area of future investigation. We also found that those sensors which were not capable of measuring temperatures colder than -20°C were not able to collect zenith sky temperature data in Socorro, New Mexico. However, at a lower elevation and less arid region, zenith sky temperatures rarely fall below -20°C [e.g. Mims et al. (2011)], and those sensors may be effectively utilized for TPW monitoring

280 As we continue the study of the relationship between zenith sky temperature and precipitable water, we plan on developing an autonomous sensor module. This module would not only enable consistent temperature measurement times, but will also facilitate an expansion of this project with more measurement sites. Additional measurement sites will increase our capability

to analyze the relationship between zenith sky temperature and precipitable water in different climate zones. We are also de-
veloping plans to work with schools to continue manual data collection in different parts of the American West to help advance

285 science learning while collecting data from regions with different elevations and precipitation profiles. Current efforts are fo-
cused on testing and optimizing a machine learning algorithm (more specifically a Support Vector Machine) to predict a binary
set of weather conditions, clear sky or overcast, based on zenith sky temperature and TPW data. These predictive models will
have the capabilities to further quantify the aforementioned relationship by applying common statistical metrics, and will be
the subject of a future paper.

290 **Appendix A**

This Appendix presents two supplementary figures that support discussions about variability in TPW and spectral passbands
of our instruments.

Figure A1 shows a comparison of surface relative humidity measured at Socorro, NM for the first halves of 2019 and 2020,
along with the corresponding T_b and TPW measurements analyzed over same two time periods. We find that RH values in late

295 spring and early summer of 2020 were much lower than those observed in 2019. Similarly, TPW values in Spring-Summer
2019 were lower in 2020 compared with 2019. However, measured values of T_b did not undergo a proportional change so that
the 2019 and 2020 relationships show small differences that can be seen in the fits. The reductions in RH and TPW appear to
be consistent with the La Nina pattern seen in 2020, although a more complete analysis would require more years of T_b and
TPW measurements.

300
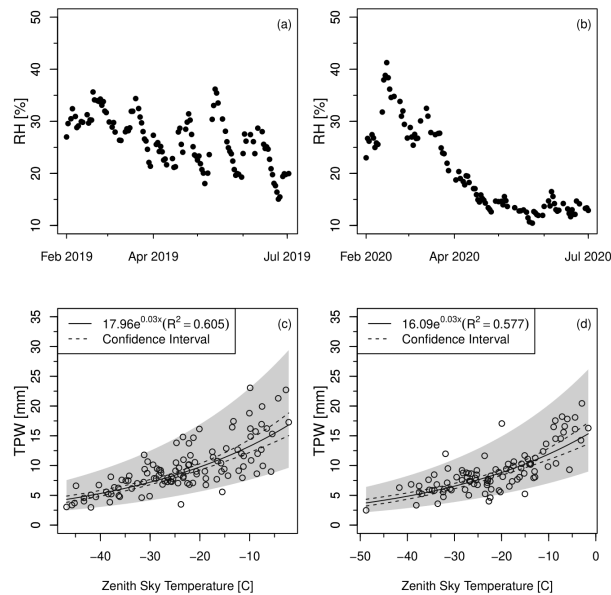
Figure A1. Top two plots show time series of surface relative humidity measured at Socorro, New Mexico. The left plot shows the period from February to July 2019, and the right plot shows the values for February-July 2020. The bottom two plots show the corresponding TPW and zenith sky temperatures for the same periods in 2019 (left) and 2020 (right).
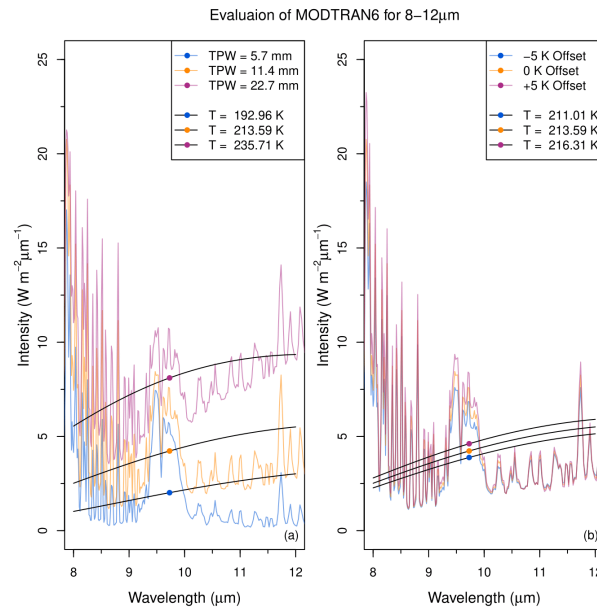
Figure A2. (Left) Downward radiances at the surface, between 8 and 12 μm, computed using MODTRAN6 with a midlatitude summer model atmosphere. Water vapor was uniformly scaled to produce a TPW of 5.7 mm (blue), 11.4 mm (orange), and 22.7 mm (purple), with all other model parameters held constant. Also plotted are blackbody curves for three different temperatures (black), with each curve having the same integrated radiance as the corresponding MODTRAN6 radiance. (Right) Same as Left but for uniform changes in atmospheric temperature of ± 5 K with water vapor held constant at TPW=11.4 mm. Equivalent blackbody curves and temperatures are also shown.

Figure A2 shows the results of MODTRAN6 calculations as described above in Sect. 4. In this case the spectral passband is assumed to be between 8 and 12 micrometers, and we find a corresponding decrease in effective brightness temperatures compared to those shown in Fig. 6. The results confirm our hypothesis that the lower temperatures observed by the FLIR i3 instruments are primarily due to differences in spectral passbands. Furthermore, we find a much reduced sensitivity to air temperature within this passband, suggesting that this kind of instrument could provide a more direct means of monitoring TPW, but only for climate regimes where mean humidities are sufficiently large so that observed sky temperatures would fall within the measurement temperature range for this instrument.

Code and data availability. The data that support the findings of this study are available from https://doi.org/10.6084/m9.figshare.12712814. The model code that was used in this study are available from https://doi.org/10.5281/zenodo.4587475

Author contributions. Vicki Kelsey conducted most of the zenith sky temperature measurements and developed the methods used for estimating local TPW from NWS data. Sarah Riley developed the analysis codes and prepared all figures in the paper. Kenneth Minschwaner assisted with measurement logistics and developed the simple linearized model. All three authors contributed equally to writing the paper.

Competing interests. The authors declare that they have no conflict of interest.

Acknowledgements. The authors would like to acknowledge the New Mexico Tech Physics Department and the Langmuir Laboratory for Atmospheric Research for their technical support of this project. The authors especially wish to thank Sooraj Bhatia, Christopher Baca, Brandon Phelps-Romero, Steve White, Fernando Rivera, Damon Apps, Eloise Apps, and Charles Apps for assisting with zenith sky and ground temperature measurements. We thank Dr. David Meier for useful discussions and acknowledge Altagracia Lujan from the New Mexico Tech Physics Department for her administrative support during this project.

References

320   Anderson, G. P.: AFGL atmospheric constituent profiles (0-120km), Air Force Geophysics Laboratory, 1986.

Berk, A., Conforti, P., Kennett, R., Perkins, T., Hawes, F., and van den Bosch, J.: MODTRAN6: a major upgrade of the MODTRAN radiative transfer code, in: Algorithms and Technologies for Multispectral, Hyperspectral, and Ultraspectral Imagery XX, edited by Velez-Reyes, M. and Kruse, F. A., vol. 9088, pp. 113 – 119, International Society for Optics and Photonics, SPIE, https://doi.org/10.1117/12.2050433, 2014.

325   Burroughs, W. J.: The Water Dimer: A Meteorologically Important Molecular Species, Weather, 34, 233–237, https://doi.org/10.1002/j.1477-8696.1979.tb05335.x, 1979.

Chen, B., Dai, W., Liu, Z., Wu, L., Kuang, C., and Ao, M.: Constructing a precipitable water vapor map from regional GNSS network observations without collocated meteorological data for weather forecasting, Atmospheric Measurement Techniques, 11, 5153–5166, https://doi.org/10.5194/amt-11-5153-2018, 2018.

330   FLIR Systems Inc.: Technical Data FLIR i3, FLIR Systems Inc., 27700 SW Parkway Ave., Technical Manual, 2012.

Gradinarsky, L., Johansson, J., Bouma, H., Scherneck, H.-G., and Elgered, G.: Climate monitoring using GPS, Physics and Chemistry of the Earth, Parts A/B/C, 27, 335 – 340, https://doi.org/10.1016/S1474-7065(02)00009-8, Geodesy and Meteorology, 2002.

Harbor Freight Tools: AMES Instruments Infrared Thermometer, Harbor Freight Tools, 3491 Mission Oaks Blvd, Technical Manual, 2017.

Hogg, D. C., Guiraud, F. O., Snider, J. B., Decker, M. T., and Westwater, E. R.: A Steerable Dual-Channel Microwave Radiometer for

335   Measurement of Water Vapor and Liquid in the Troposphere, J. Climate Appl. Meteor., 22, 789–806, https://doi.org/10.1175/1520-0450(1983)022<0789:ASDCMR>2.0.CO;2, 1983.

Kelsey, V. and Riley, S.: TPW and Zenith Sky Temperature Data for Socorro, NM, Figshare [data set], https://doi.org/10.6084/m9.figshare.12712814, 2021.

Liljegren, J. C.: Two-Chanel Microwave Radiometer for Observations of Total Column Precipitable Water Vapor and Cloud Liquid Water

340   Path, in: Fifth Symposium on Global Change Studies, 1994.

Marcus, S., Kim, J., Chin, T., Danielson, D., and Laber, J.: Influence of GPS Precipitable Water Vapor Retrievals on Quantitative Precipitation Forecasting in Southern California, J. Appl. Meteor. Climatol., 46, 1828–1839, https://doi.org/10.1175/2007JAMC1502.1, 2007.

Maussion, F., Scherer, D., Mölg, T., Collier, E., Curio, J., and Finkelnburg, R.: Precipitation Seasonality and Variability over the Tibetan Plateau as Resolved by the High Asia Reanalysis*, J. Climate, 27, 1910–1927, https://doi.org/10.1175/JCLI-D-13-00282.1, 2014.

345   Means, J. D. and Cayan, D.: Precipitable Water from GPS Zenith Delays Using North American Regional Reanalysis Meteorology, J. Atmos. Oceanic Technol., 30, 485–495, https://doi.org/10.1175/jtech-d-12-00064.1, 2013.

Mims, F. M., Chambers, L. H., and Brooks, D. R.: Measuring Total Column Water Vapor by Pointing an Infrared Thermometer at the Sky, Bull. Amer. Meteor. Soc., 92, 1311 – 1320, https://doi.org/10.1175/2011bams3215.1, 2011.

Minschwaner, K., Varney, L., and Starke, V.: Effect of aerosols on surface UV at Socorro, New Mexico: measurements based on

350   global irradiances and a direct sun photometer, in: Ultraviolet Ground- and Space-based Measurements, Models, and Effects, edited by Slusser, J. R., Herman, J. R., and Gao, W., vol. 4482, pp. 265 – 270, International Society for Optics and Photonics, SPIE, https://doi.org/10.1117/12.452927, 2002.

Raj, P. E., Devara, P. C. S., Maheskumar, R. S., Pandithurai, G., Dani, K. K., Saha, S. K., Sonbawne, S. M., and Tiwari, Y. K.: Results of Sun Photometer–Derived Precipitable Water Content over a Tropical Indian Station, J. Appl. Meteor., 43, 1452–1459,

355   https://doi.org/10.1175/jam2149.1, 2004.

Randel, D. L., Vonder Haar, T. H., Ringerud, M. A., Stephens, G. L., Greenwald, T. J., and Combs, C. L.: A New Global Water Vapor Dataset, Bull. Amer. Meteor. Soc., 77, 1233–1246, https://doi.org/10.1175/1520-0477(1996)077<1233:ANGWVD>2.0.CO;2, 1996.

Riley, S. and Kelsey, V.: Precipitable-Water Model Analysis Tool: Cirrus, Zenodo [code], https://doi.org/10.5281/zenodo.4587475, 2021.

Robles, M. C., Amos, H. M., Dodson, J. B., Bouwman, J., Rogerson, T., Bombosch, A., Farmer, L., Burdick, A., Taylor, J., and Chambers, L. H.: Clouds around the World: How a Simple Citizen Science Data Challenge Became a Worldwide Success, Bull. Amer. Meteor. Soc., 101, E1201 – E1213, https://doi.org/10.1175/BAMS-D-19-0295.1, 2020.

Ross, R. J. and Elliott, W. P.: Tropospheric Water Vapor Climatology and Trends over North America: 1973–93, J. Climate, 9, 3561–3574, https://doi.org/10.1175/1520-0442(1996)009<3561:twvcat>2.0.co;2, 1996.

Salby, M. L.: Fundamentals of atmospheric physics, Elsevier, 1996.

Schmit, T. J., Griffith, P., Gunshor, M. M., Daniels, J. M., Goodman, S. J., and Lebair, W. J.: A Closer Look at the ABI on the GOES-R Series, Bull. Amer. Meteor. Soc., 98, 681 – 698, https://doi.org/10.1175/BAMS-D-15-00230.1, 2017.

Schmit, T. J., Lindstrom, S. S., Gerth, J. J., and Gunshor, M. M.: Applications of the 16 spectral bands on the Advanced Baseline Imager (ABI)., Journal of Operational Meteorology, 06, 33–46, https://doi.org/10.15191/nwajom.2018.0604, 2018.

Schober, P., Boer, C., and Schwarte, L. A.: Correlation Coefficients: Appropriate Use and Interpretation, Anesthesia & Analgesia, 126, 2018.

Smith, S. and Toumi, R.: Measuring Cloud Cover and Brightness Temperature with a Ground-Based Thermal Infrared Camera, J. Appl. Meteor. Climatol., 47, 683–693, https://doi.org/10.1175/2007JAMC1615.1, 2008.

Stephens, G. L.: Remote sensing of the lower atmosphere: an introduction, Oxford University Press, 1994.

Taylor, J.: An Introduction to Error Analysis: The Study of Uncertainties in Physical Measurements, ASMSU/Spartans.4.Spartans Textbook, University Science Books, 1997.

Thomas, G. E., Stamnes, K. H., and Stamnes, J. J.: Radiative transfer in the atmosphere and ocean, Cambridge University Press, 1999.

Thomason, L. W.: Extinction of Near Infrared Solar Radiation as a Means for Remote Determination of Atmospheric Water Vapor, Ph.D. thesis, The University of Arizona, 1985.

Thome, K. J., Herman, B. M., and Reagan, J. A.: Determination of Precipitable Water from Solar Transmission, J. Appl. Meteor., 31, 157–165, https://doi.org/10.1175/1520-0450(1992)031<0157:dopwfs>2.0.co;2, 1992.

Wang, J., Zhang, L., Dai, A., Van Hove, T., and Van Baelen, J.: A near-global, 2-hourly data set of atmospheric precipitable water from ground-based GPS measurements, Journal of Geophysical Research: Atmospheres, 112, 2007.

Wang, R., Fu, Y., Xian, T., Chen, F., Yuan, R., Li, R., and Liu, G.: Evaluation of Atmospheric Precipitable Water Characteristics and Trends in Mainland China from 1995 to 2012, J. Climate, 30, 8673–8688, https://doi.org/10.1175/JCLI-D-16-0433.1, 2017.

Yang, L. and Smith, J.: Sensitivity of Extreme Rainfall to Atmospheric Moisture Content in the Arid/Semiarid Southwestern United States: Implications for Probable Maximum Precipitation Estimates, J. Geophys. Res.: Atmospheres, 123, 1638–1656, https://doi.org/10.1002/2017JD027850, 2018.

Zhao, P., Li, Y., Guo, X., Xu, X., Liu, Y., Tang, S., Xiao, W., Shi, C., Ma, Y., Yu, X., Liu, H., Jia, L., Chen, Y., Liu, Y., Li, J., Luo, D., Cao, Y., Zheng, X., Chen, J., Xiao, A., Yuan, F., Chen, D., Pang, Y., Hu, Z., Zhang, S., Dong, L., Hu, J., Han, S., and Zhou, X.: The Tibetan Plateau Surface-Atmosphere Coupling System and Its Weather and Climate Effects: The Third Tibetan Plateau Atmospheric Science Experiment, Journal of Meteorological Research, 33, 375–399, https://doi.org/10.1007/s13351-019-8602-3, 2019.